



Preparation, infrared emissivity and thermochromic properties of Co doped ZnO by solid state reaction

Yongmei Zhu*, Guoyue Xu, Tengchao Guo, Haili Hou, Shujuan Tan

College of Material Science and Technology, Nanjing University of Aeronautics and Astronautics, Jiang Jun Street 29, Nanjing 211106, China



ARTICLE INFO

Article history:

Received 29 March 2017

Received in revised form

19 May 2017

Accepted 24 May 2017

Available online 25 May 2017

Keywords:

Infrared emissivity

Thermochromic

Co-doped ZnO

Solid-state reaction

ABSTRACT

In this paper, green $Zn_{1-x}Co_xO$ nanopowders were synthesized via solid-state reaction at different calcination temperatures. The effects of sintering temperature on structure, morphologies, color and infrared emissivity was investigated by X-ray diffraction (XRD), scanning electron microscopy (SEM), energy dispersive spectroscopy (EDS), X-ray photoelectron spectroscopy (XPS), UV-visible absorption spectroscopy, Raman spectroscopy and IR-2 dual-band infrared emissometer, respectively. The results show that the as-synthesized samples have hexagonal wurtzite structure and meantime the peaks of the secondary phase, Co_3O_4 , were observed when the sintering temperature is below 900 °C. The sintering temperature plays a vital important role in crystallite sizes, lattice parameters, volume of the unit cell as well as microstructure. According to the EDS results, Zn ions were substituted by the Co ions in the ZnO lattice where Co ions present in the +2 state indicated via XPS analysis. Additionally, UV-visible absorption spectra shows that absorption edge have a red shift while the corresponding energy band gap of the semiconductor nanoparticles decrease with the increasing sintering temperature, which affects the thermochromic characteristics of materials significantly. The infrared emissivity is related to the microstructure, grain size, conductivity and lattice vibration.

© 2017 Elsevier B.V. All rights reserved.

1. Introduction

Recently, thermochromic materials have received significant attention due to the potential utilization in various sectors such as space, industry and military fields [1,2]. When they are applied in industry fields, it can not only as temperature indicating coatings to monitor instruments temperature, but also can as building coatings to provide cool tones in summer and warm tones in winter and therefore to decrease the energy consumption of a building environment in any seasons [3]. The variable emissivity coatings, which is based on thermochromism, have great application prospects to spacecraft thermal control, owing to the lightness, low energy consumption and facility [4,5]. The smart thermo-responsive coatings can be used as chameleon coatings in military technology to change the colors of military equipment to match its surroundings, and then decrease the probability being detected [6,7].

According to the literatures, the materials used to synthesize thermochromic materials mainly focus on VO_2 [8] and $La_{1-x}Sr_xMnO_3$ [9]. Nevertheless, it is evident that VO_2 is not only

expensive but also dangerous. As for $La_{1-x}Sr_xMnO_3$, it usually has high solar absorptance (over 0.8) and needs sophisticated instruments to control assistantly. Consequently, both of them are not suitable to fabricate thermochromic materials.

As a non-toxic, cheap, readily available and environmentally white pigment, zinc oxide with low light absorbance and high radiation dispersion in the visible regio, which can be used in sun-screen compositions to block UV radiation. Besides, the high reflectance appears in near - infrared region makes it suitable candidate for space applications [10]. It has wide band gap energy (3.3 eV) at room temperature [11] and high excitonic binding energy (60 meV) [12]. As an important n-type semiconductor material, ZnO has received extensive attention because of its remarkable optical, magnetic, and electrical properties [13–17]. The transition metal elements doped ZnO matrix is one of the most important methods to modify the electronic structure and characteristics of the host material [18–20]. Among all of the transition metals, Co has been widely employed because of its variable oxidation state, large magnetic and high solubility limit in ZnO due to the similar ionic radius (0.072 nm) with Zn^{2+} atom (0.074 nm) [21–24]. In the past several years, many studies referred to Co-doped ZnO have focused on the magnetic properties [25–27]. The properties of variable emissivity and thermochromic, however, are neglected.

* Corresponding author.

E-mail address: 1105249397@qq.com (Y. Zhu).

There is no doubt that emissivity is one of the important physical properties of materials, which have wide applications in various fields. The materials with high emissivity at high temperature can be used in furnaces lining, supersonic aircraft and other fields to save energy or decrease the temperature by radiation [28,29]. Low infrared emissivity (LIE) materials can prevent targets from being detected by infrared detectors when coated on the surface of military equipments [30–32]. However, thermochromic characteristics and variable emissivity properties of ZnO-based materials were scarcely reported so far.

In this paper, we conducted a simple solid-state reaction to synthesize green $Zn_{1-x}Co_xO$ nanopowders successfully and studied the effects of calcination temperatures on its crystal structures, morphologies as well as infrared emissivity. Besides, the color of $Zn_{1-x}Co_xO$ nanopowders can gradually change from green to yellow with the increase of testing temperature and the changes are reversible.

2. Experimental details

The doped oxides $Zn_{1-x}Co_xO$ were prepared by solid-state reaction. Raw ZnO powders (9.503 g) and Co_3O_4 powders (0.497 g) were mixed before calcination. This mixture was gently ground in an agate mortar for homogenisation. The obtained powders were calcined for 20 h in furnace at designed temperatures from 700 °C to 1100 °C with a step of 100 °C with a constant heating rate of 4 °C/min until reach the annealing temperature. After annealed, the powder was cooled to room temperature gradually in furnace. Finally, the pre-treated $Zn_{1-x}Co_xO$ powders with different annealing temperature were obtained.

The decomposition temperature of the Co_2O_3 was investigated by simultaneous thermogravimetry and differential scanning calorimetry (TG-DSC), which was performed with a temperature-increasing rate of 10 °C/min using a simultaneous TG-DSC STA449C model analyzer in N_2 atmosphere at 1100 °C. The crystalline phases of the sintered powders were examined by x-ray diffraction using $CuK\alpha$ radiation (XRD Rigaku, D/max-RA) from 20° to 80° (2θ). The presence of Zn, Co, and O in the samples was confirmed by the energy dispersive spectroscopy (EDS). The chemical state of Co in $Zn_{1-x}Co_xO$ samples was studied by Thermo Scientific X-ray Photoelectron Spectrometer (XPS, PHI-5000 Versaprobe) with a monochromatic Al $K\alpha$ source with 1486.6 eV of energy and 150 W of power. The microstructure of samples was characterized by scanning electron microscopy (SEM, FEI SIRION-100). To determine the optical band gap of different samples, the optical absorption measurements were performed with a Shimadzu 2450 UV–VIS spectrophotometer and the investigated wavelength ranged from 200 to 800 nm. Raman spectra from 100 cm⁻¹ to 700 cm⁻¹ were acquired at room temperature using a Jobin-Yvon T64000 Triple-mate instrument. The electrical resistivity of the $Zn_{1-x}Co_xO$ nanoparticles in room temperature was measured with the two-electrode method in AC circuit (FT-303 serial resistivity tester). The infrared emissivity in the range of 3–5 μm in different temperature was detected by an infrared emissometer (IR-2 dual-band emissometer, Shanghai Institute of Technical Physics, CAS, China). The temperature dependence of infrared emissivity was performed using BC-1 temperature control instrument (Shanghai Institute of Technological Physics, China). The testing temperature can range from 20 °C to 700 °C with a heating rate of 20 K·min⁻¹.

3. Results and discussion

3.1. Thermogravimetry and differential scanning calorimetry study (TG-DSC)

TG-DSC analysis result of the Co_2O_3 powders are shown in Fig. 1.

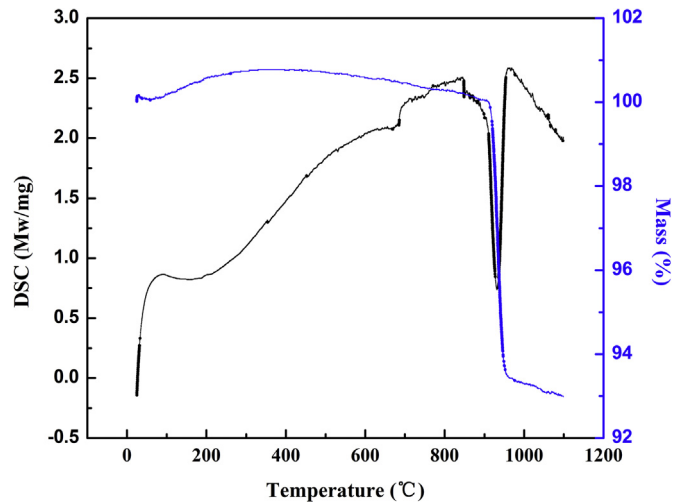


Fig. 1. TG-DSC results of Co_2O_3 .

The pronounced loss of weight can be observed at 900 °C, which is due to the fact that Co_2O_3 powders decompose into CoO at high temperature condition. Correspondingly, a remarkable endothermic peak in DSC curve is observed at the temperature around 900 °C. In addition, a small endothermic peak can be observed around 700 °C because of the decomposition of Co_2O_3 into Co_3O_4 . It indicates that there are two step degradation processes in the sample. The DSC result provides useful information to determine the appropriate starting temperature for the calcination process. Therefore, from the DSC, it can be seen that the properly annealing temperature is 900 °C, which ensures the completely thermal decompose of Co_2O_3 . The result is similar to that reported by Z.D. Nan et al. [33].

3.2. X-ray diffraction study (XRD)

Fig. 2 gives the XRD spectrums of Co^{2+} ions doped in ZnO nanoparticles. Clearly, all the peaks well match with the JCPDS date of pure ZnO (card no.36-1451) with space group of p63mc, indicating that all samples possess a wurtzite (hexagonal) zincite crystal structure with a more preferential orientation along the c-axis perpendicular. However, a small amount of impurity peaks are captured arisen from the secondary phase (Co_3O_4) when sintered at 800 °C or below. The secondary phase may be due to the incompletely decomposition of Co_2O_3 below 900 °C. This result is consistent with TG-DSC study. The RIR method was employed to calculate the phase composition of the hybrids quantitatively, according to the following equations [34,35]:

$$W_a = \frac{I_a}{I_a + (I_b / (RIR_b / RIR_a))}$$

$$W_b = \frac{I_b}{I_b + (I_a / (RIR_a / RIR_b))} = 1 - W_a$$

The weight ratio of Co_3O_4 at calcination temperatures of 700 °C and 800 °C is 3.7% and 2.8%, respectively. This also implies that higher temperature is helpful for Co^{2+} doping into ZnO lattice. Moreover, different starting materials, for example CoO or Co, may need different calcination temperature to achieve pure single ZnO phase [36,37].

Fig. 2(b) shows that the higher the temperature is, the diffraction peaks have a little shift to higher angles, and their values are tabulated in Table 1. As we all know the radius of Co^{2+} (0.72 Å) is

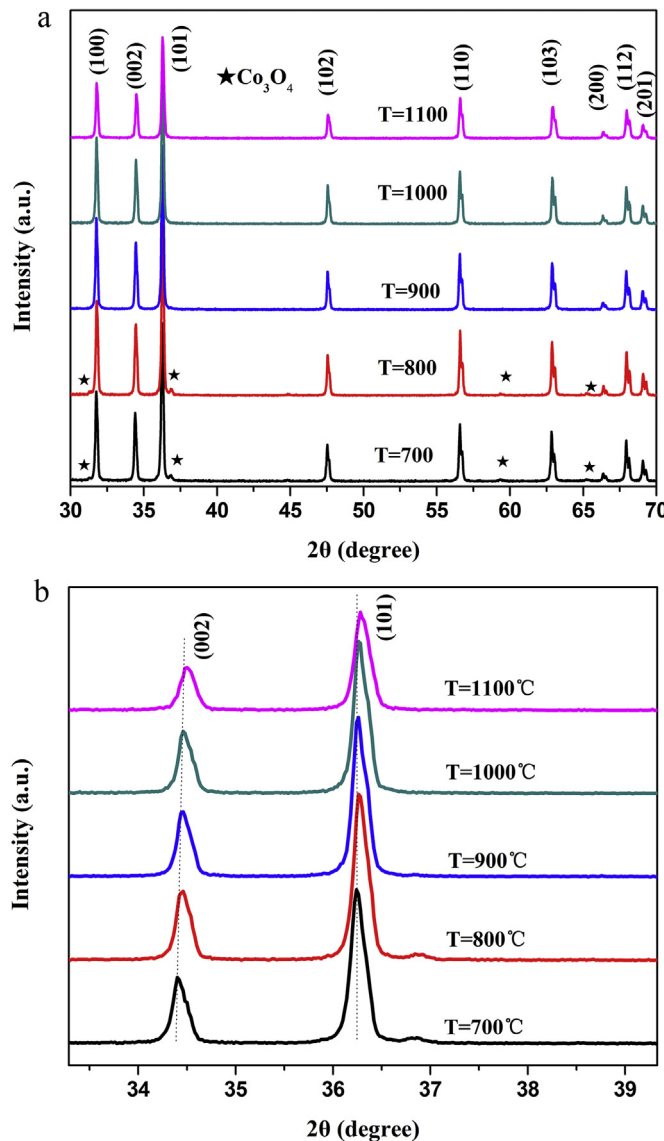


Fig. 2. (a) XRD patterns of Zn_{1-x}Co_xO nanoparticles at different calcination temperatures; (b) magnified XRD patterns of samples.

smaller than that of Zn²⁺ (0.74 Å). According to the Bragg's law [38].

$$2d \sin\theta = n\lambda$$

where θ is the diffraction angle, λ is the incident wavelength ($\lambda = 1.5406$ Å) and n is the diffraction series ($n = 1$ in normal conditions). For hexagonal wurtzite structure of ZnO, the interplanar spacing d is related to the Miller indices h , k and l as well as

Table 1
Structure parameters of the sample.

T(°C)	Position of (002) peak (degree)	Position of (101) peak (degree)	Intensity of (101) peak (a.u.)	FWHM degree	D ₀₀₂ (nm)	Volume (Å)	Lattice parameters	c/a ratio	
					a(Å)	c(Å)			
700	34.401	36.239	3328	0.146	56.969	47.64	3.25024	5.20719	1.60209
800	34.440	36.260	3209	0.142	58.578	47.59	3.25033	5.20438	1.60119
900	34.441	36.258	3046	0.138	60.276	47.60	3.25057	5.20312	1.60068
1000	34.460	36.261	2944	0.136	61.166	47.58	3.25065	5.20152	1.60015
1100	34.481	36.271	1849	0.150	55.460	47.56	3.24993	5.19951	1.59988

lattice parameters 'a' and 'c' by the following equation [39].

$$\frac{1}{d^2} = \left\{ \frac{4}{3} \left(\frac{(h^2 + k^2 + hk)}{a^2} + \frac{l^2}{c^2} \right) \right\}$$

The calculated lattice parameters 'a' and 'c' and c/a ratio of pure and Co²⁺ doped ZnO nanoparticles are shown in Table 1. With the increasing of temperature, the lattice parameter 'a' is found a little increasing, whereas 'c' parameter is found decreasing. The higher temperature makes the bigger doping concentration of Co²⁺ into ZnO, which results in the shift of 2θ into large angles. Actually, the replacement of Zn ions by Co ions decreases the lattice constant c and this shrink in the z-axis of the unit cell causes an elongation in the x axis, so it leads to a little increase of the lattice constant a. These results are in good agreement with those reported earlier [40,41].

The average crystallite size (D) of nanoparticles was calculated from the Debye Scherrer's equation [42].

$$D = \frac{0.9\lambda}{\beta \cos\theta}$$

where, D is the crystallite size. λ is the wavelength of X-ray ($\lambda = 1.54056$ Å), θ is the Bragg's angle and β is the full width at half maximum of the most intense diffraction peaks. As shown in Table 1, the decrease of the full width at half maximum of the diffraction peak reveals that the attained particle size has increased from 56.969 nm to 61.166 nm with the increasing of the calcination temperature from 700 °C to 1000 °C, which could be attributed to the fact that as the temperature went high, many neighbouring particles tended to fuse together to form larger particle size by melting their surfaces [43]. When the sintering temperature is at 1100 °C, the average crystallite size is found to decrease to 55.460 nm. This phenomenon could be explained as follows: the distortion in the host ZnO lattice [44]. The introduction of foreign impurity contributes to the decrease of nucleation rate and the growth rate is decreased subsequently. A. Goktasa et al. [45] and S.D. Birajdar et al. [67] have reported that the crystalline size decreases with increase of Co²⁺ content in ZnO.

The volume of the unit cell was calculated by using the following equation:

$$V = \frac{\sqrt{3}}{2} a^2 c$$

where V is the volume of the hexagonal unit cell, 'a' and 'c' is the lattice parameter. It was found that the volume of the unit cell decreases with increasing of sintering temperature, which is displayed in Table 1.

From the XRD patterns in Fig. 2(b), it is found that the intensity of the (101) plane for all the samples gradually decreases with the increasing of sintering temperature, which indicates that the dopant of Co ions substitute in the inner lattice of Zn ions [46,47].

When the sintering temperature is 1100 °C, the diffraction peak intensities is weakened, which may be due to the weakened crystalline quality.

3.3. Scanning electron microscopy (SEM)

Fig. 3A–E shows the morphology of $Zn_{1-x}Co_xO$ at various temperatures with the same magnification. The SEM images imply that the temperature plays an important role in the technical process of morphology-controlled synthesis. It can be observed that the samples consist of spherical particles and construct a loosely porous structure when the sintering temperature is at 700 °C. The grain size of powders appears to increase with higher sintering temperature, and the block grains are formed when the sintering temperature reaches 1000 °C. It is believed that the increase of grain size is due to the effects of the liquid phase sintering process.

And the liquid phase helps facilitate ion diffusion and enhances the grain growth mechanism during sintering process [48]. The grain growth could bring about the loss of specific surface area. However, when the sintering temperature continues rising to 1100 °C, the particle diameter has no apparent growth.

3.4. Energy dispersive spectrometer

In order to analyze the chemical compositions and amount of Co contents in doped ZnO, the powders were examined by EDS and their spectrums are shown in **Fig. 4**. All samples have one zinc peak at 1.01 KeV and O signals at 0.52 KeV. The cobalt peaks at 0.78 KeV and 6.94 KeV are observed in all samples. These verify the presence of Co ions in ZnO and suggest that the Co ions substituted the Zn ions in the ZnO lattice. The percentages of Co ions in all samples are less than the target composition 2.5%. This is probably due to the

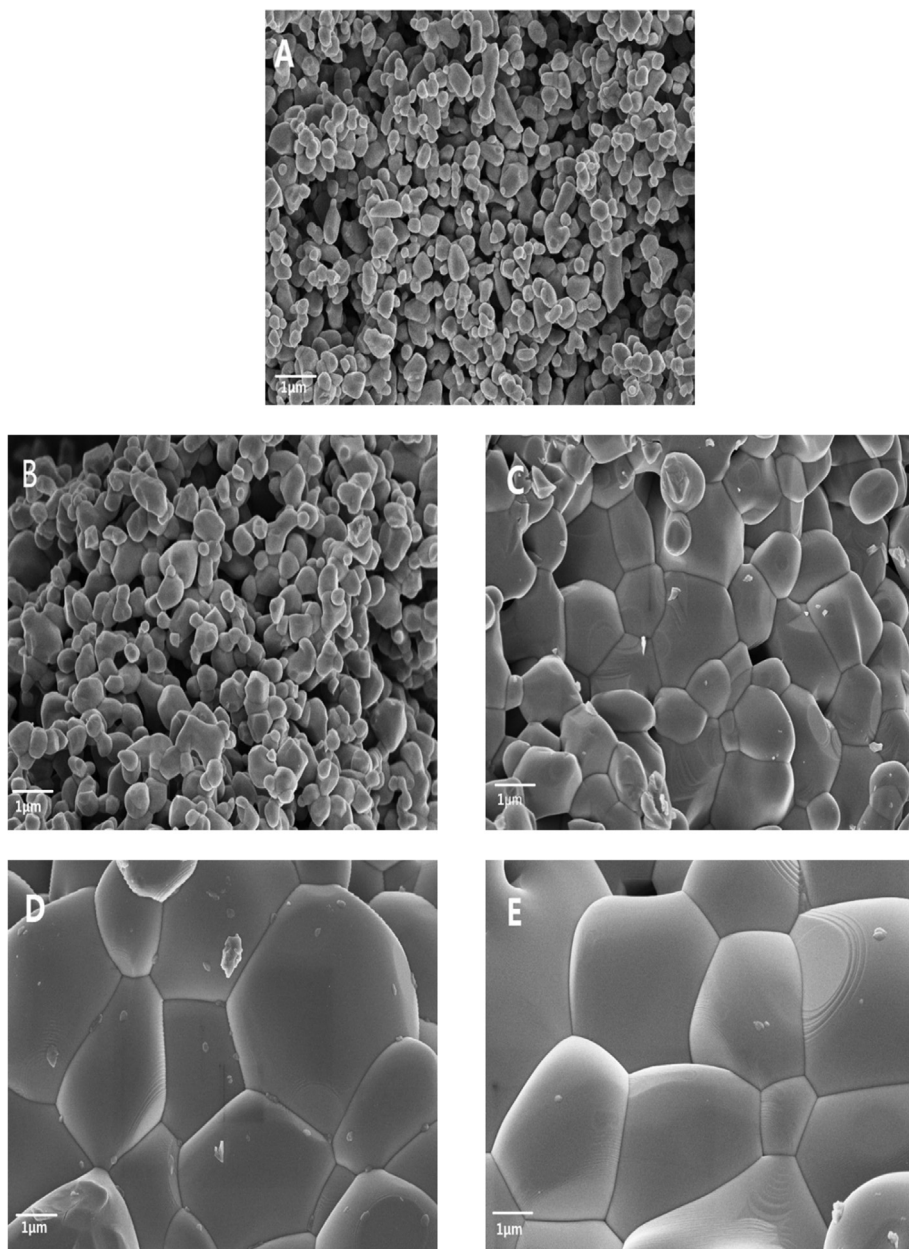


Fig. 3. SEM images of the $Zn_{1-x}Co_xO$ nanoparticles with different sintering temperatures: A 700 °C; B 800 °C; C 900 °C; D 1000 °C; E 1100 °C.

decomposition and volatilization of Co_3O_4 at high temperatures and the low detection limitation in SEM-EDS measurement system. The concentration of Co^{2+} at calcination temperatures of 700 °C, 800 °C, 900 °C, 1000 °C and 1100 °C is about 0.57%, 0.99%, 1.46%, 1.58% and 2.30%, respectively. It can be seen that with the increase of calcination temperature, the concentration of Co^{2+} become larger, which is consistent with XRD study as well.

3.5. XPS analysis

The oxidation states of Co, Zn, and O in Co-doped ZnO samples have been detected via X-ray photoelectron spectra (XPS). The results of the sample which calcined at 1000 °C are shown in Fig. 5(a).

In the XPS spectra, all the binding energy of relevant elements in the sample system is referenced to C 1s hydrocarbon signal at 284.8 eV. As can be seen from the high-resolution Co 2p spectrum of the sample, the obtained binding energies at 781.0 eV and 796.4 eV are attributed to $\text{Co } 2\text{p}_{3/2}$ and $\text{Co } 2\text{p}_{1/2}$, respectively. It indicates that the oxidation number of Co in the ZnO lattice is 2+. It should be noted that each of the two peaks in the spectrum is followed by satellite peak, which is due to the exchange between valence electrons and core hole, resulting in the change of voltage. It can be seen that the valence electrons are created by the core hole [49], and this is a feature of Co^{2+} ions. The binding energy of $\text{Co } 2\text{p}_{3/2}$ and $\text{Co } 2\text{p}_{1/2}$ signals are different from that of Co^{3+} ions 780.0 eV and 795.2 eV as well as Co metal 777.8 eV and 792.0 eV. This shows

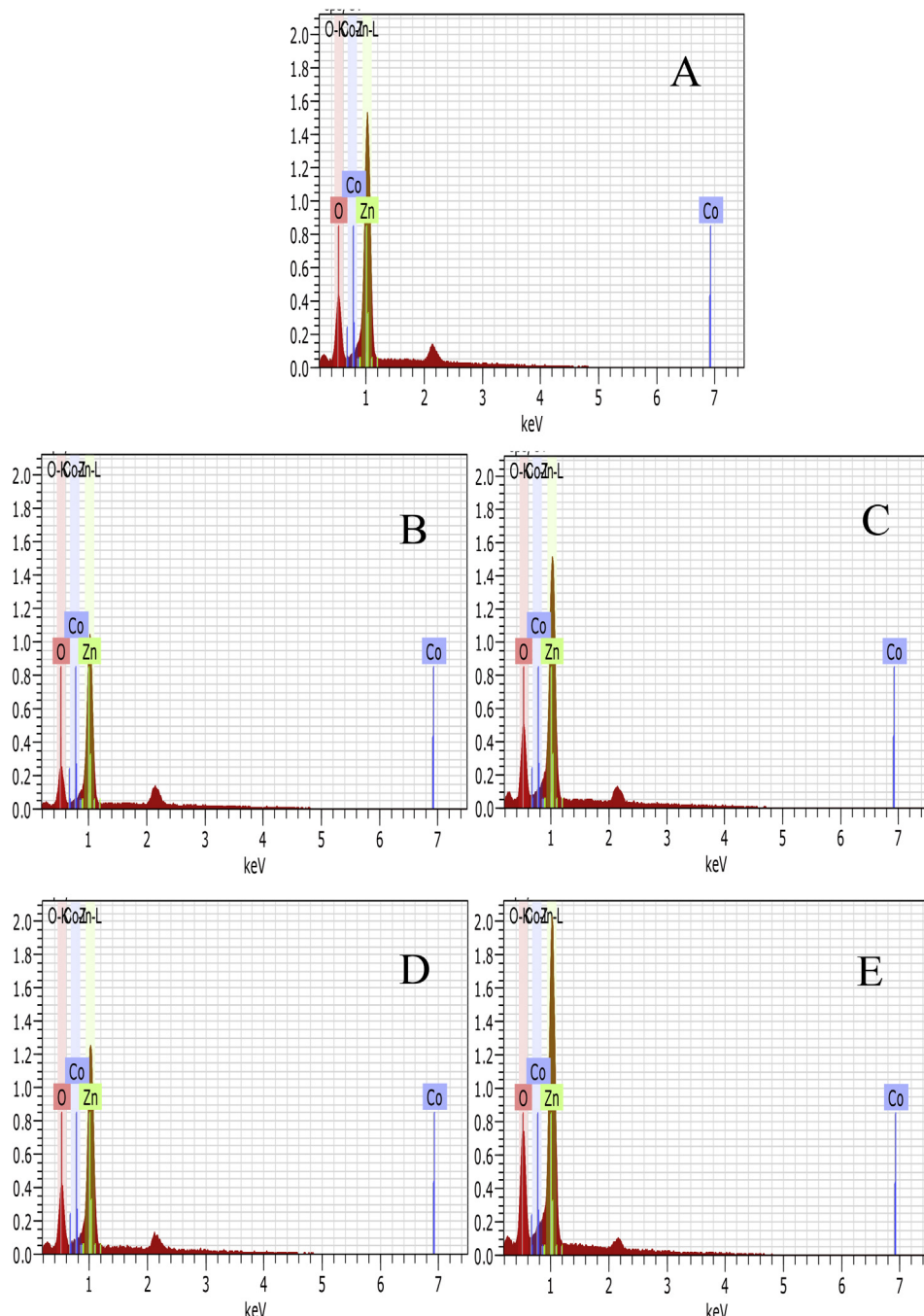


Fig. 4. EDS spectra of the $\text{Zn}_{1-x}\text{CoxO}$ powders with different calcination temperatures: A 700 °C; B 800 °C; C 900 °C; D 1000 °C; E 1100 °C.

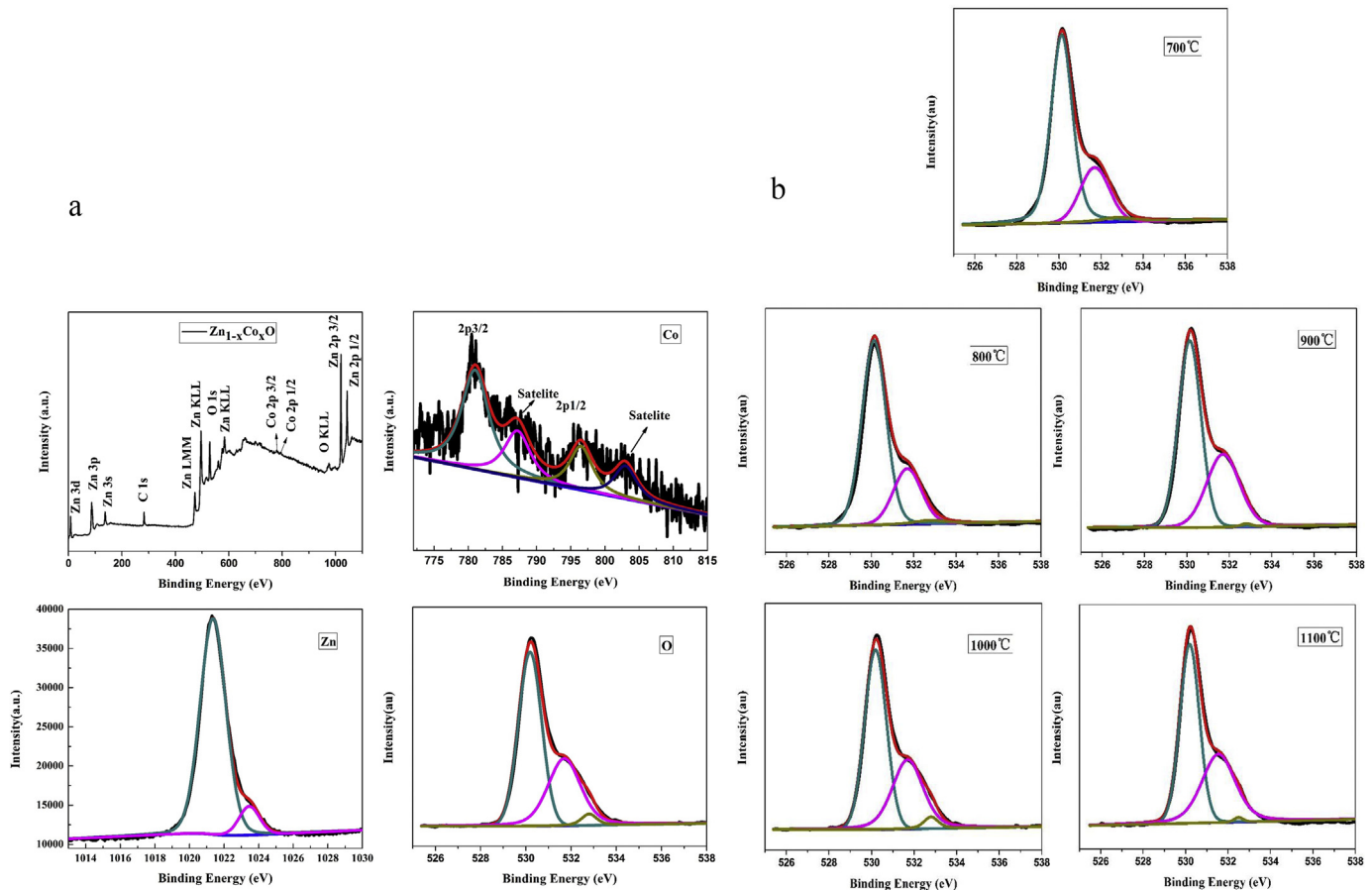


Fig. 5. (a) XPS spectra of the sample calcinated at 1000 °C; (b) the O1s spectra of different samples.

that Co dopants entered into the ZnO lattice only as Co^{2+} ions [50]. As can be seen from the O 1s signal, more than one state of O in the ZnO lattice is the main reason causing asymmetry of the O 1s peak. The state of Co doping in ZnO has been studied by using two Gaussian functions to fitting O 1s XPS spectra. The binding energy of 532.8 eV is attributed to the oxygen which is adsorbed on the surface of the ZnO powder. The highest peak in the spectra is contributed by O^{2-} ions in hexagonal wurtzite structure of ZnO. The peak at 531.7 eV is the signal of oxygen vacancies. The binding energies of Zn 2p_{3/2} and Zn 2p_{1/2} are 1021.3 eV and 1044.4 eV, which is in agreement with the standard data of zinc oxide.

Fig. 5(b) shows the O1s spectra of different samples. Their relative areas can be correlated with the contents of oxygen vacancies. It is found that the vibration peak at about 530.1 eV decreases while another peak at about 531.7 eV increase with the elevation of calcination temperatures. The area ratio of oxygen vacancies can be calculated from the XPS spectra. As shown in Table 2, the area ratio of oxygen vacancies increased from 24.86% to

42.03% with the improvement of sintering temperature from 700 °C to 1100 °C.

3.6. Raman spectra

The Raman spectra for different samples are shown in Fig. 6. The wurtzite structure of ZnO, with space group C4 6v, has four Raman-active optical phonon modes ($\text{A}_1 + \text{E}_1 + 2\text{E}_2$) and one inactive mode (B_1). The infrared active modes of A_1 and E_1 are split into longitudinal modes (LO) and transverse modes (TO). The spectral peak locates at about 333 cm^{-1} , corresponding to the multi phonon mode of ZnO. The peak at 378 cm^{-1} mode is attributed to the transverse optical mode (TO). A very weak shoulder locates at the low energy side of 437 cm^{-1} peak in pure ZnO sample, corresponding to the mode of $\text{E}_1(\text{TO})$ at 410 cm^{-1} . It disappears at high sintering temperature which is due to the disorder induced by the Co doping. As shown in Fig. 6, the sharp peak located at 437 cm^{-1} corresponds to the nonpolar optical phonon E_2 mode, which is the characteristic peak of wurtzite structure of ZnO, and that is sensitive to the crystalline quality crystal and stress of the samples. With the increase of sintering temperature, the E_2 (high) modes of the samples decreased in different degrees. That is to say, the ZnO crystal structure is destroyed by the Co substitution [51]. When the sintering temperature increases up to 1100 °C, the Raman line of E_2 (High) becomes very broad and weak, indicating decreased crystallinity. The E_2 (high) mode redshift is adequately attributed to the phonon softening caused by the in-plane lattice expansion [52]. The peak at 578 cm^{-1} is due to the defects such as oxygen vacancies and Zn interstitials. An additional peak was observed at 545 cm^{-1} .

Table 2

The area ratio of each peak in the O 1s XPS spectra for different samples.

T(°C)	Area ratio%		
	530.1(eV)	531.7(eV)	532.8(eV)
700	72.56	24.86	2.58
800	72.33	25.44	2.23
900	62.77	35.58	1.65
1000	59.10	37.63	3.27
1100	56.22	42.03	1.75

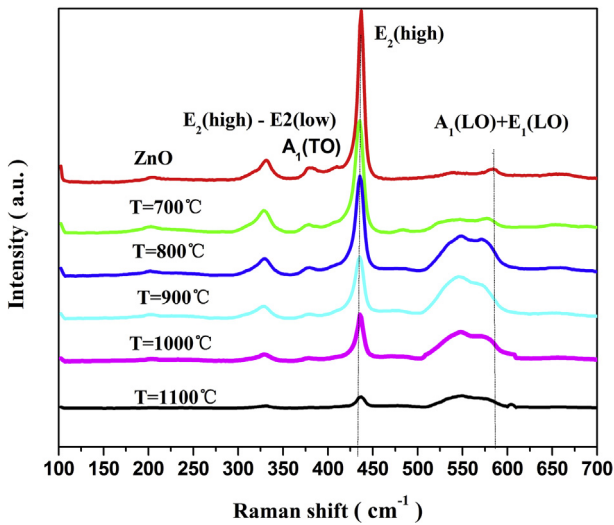


Fig. 6. Raman spectra of Zn_{1-x}CoxO samples with different sintering temperatures.

corresponding to a multiphonon peak due to the substitution of Co with Zn in the lattice.

3.7. UV-vis absorption spectra and optical band gap

To explore the optical properties and band gap of different samples, UV-vis absorption spectra was measured at room temperature. From Fig. 7(a), three absorption peaks can be observed at 565 nm, 610 nm, and 660 nm, respectively. These absorptions are attributed to the d-d transitions of the Co ions, corresponding the transitions from ⁴A₂(F) to ²E(G), ⁴A₂(F) to ²T₁(P), and ⁴A₂(F) to ²A₁(G), respectively [53]. These absorption peaks indicate that Co²⁺ ions have partially substituted Zn²⁺ ions in all the samples [54]. The absorption edge is found to red shift with increase of the sintering temperature as exhibited in Fig. 7(b).

The optical band gap of all samples can be obtained by Kubelka-Munk function [55]:

$$(\alpha h\nu)^2 = A(h\nu - E_g)$$

where, α is the absorption coefficient, h is the Planks constant, A is a constant, $h\nu$ is the photon energy and E_g is the optical energy band gap. The optical band gap energies were found to be 3.16 eV, 2.76 eV, 2.64 eV, 2.58 eV, and 2.44 eV of the Zn_{1-x}CoxO powders obtained at various calcination temperature, namely, 700 °C, 800 °C, 900 °C, 1000 °C and 1100 °C. Inspecting Fig. 7(b), it is obvious that the E_g value of all samples decrease with the increase of the calcination temperature, which mainly originated from the sp-d exchange interactions between the band electrons and the localized d electrons of the Co²⁺ ions substituting Zn²⁺ ions. The exchange interactions between s-d and p-d orbital give rise to a negative correction to the conduction-band and a positive correction to valence-band edges, which results in the decrease in band gap [56]. Additionally, the high concentration of oxygen vacancy creates an impurity level near the valence band and induces the band gap narrowing [57]. This red shift of the band gap may be also due to large lattice strain and heat treatment [58].

3.8. Colour and thermochromic analysis

The colour of pure ZnO powders is white, while Co²⁺ doped ZnO powder is green. Fig. 8(a) reveals that the green becomes darker,

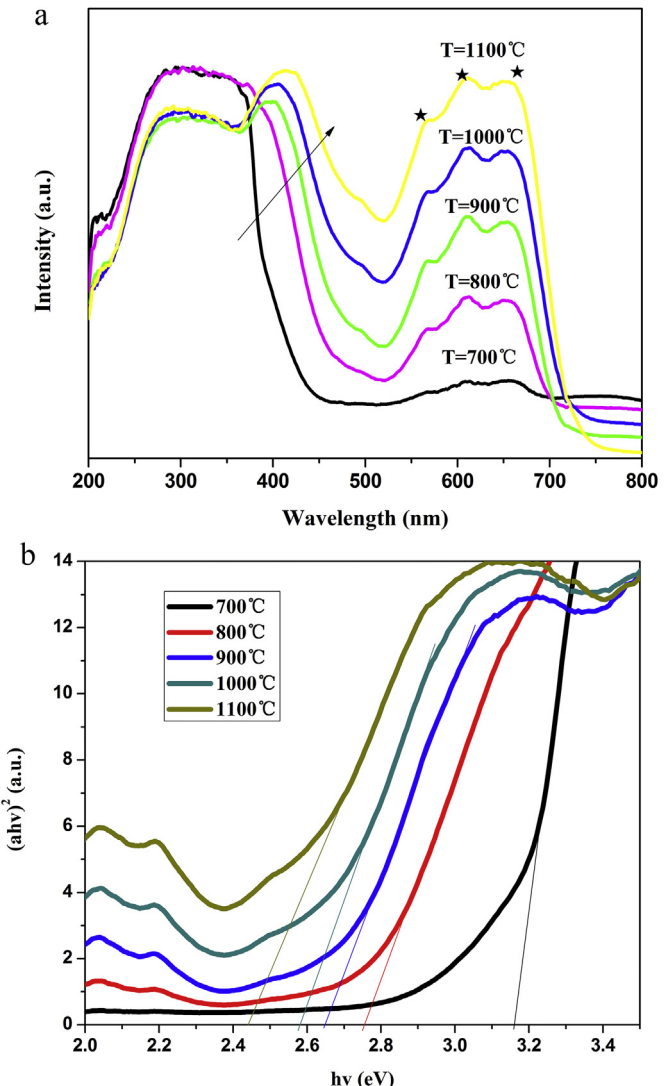


Fig. 7. (a) UV-visible absorption spectra Zn_{1-x}CoxO nanoparticles; (b) the plot of (ahv)² verses photon energy (hv) of Zn_{1-x}CoxO nanoparticles.

transiting from apple green to moss green, when the sintering temperature increases from 700 °C to 1100 °C. The color of all the samples can transformate from green to army yellow at high temperatures and the phenomenon is much more obvious with the enhancement of testing temperature. Fig. 8(b) shows the color under different test temperatures of the sample which calcinated at 900 °C. Besides, it is also interesting to note that the color-changing temperature has decreased with increasing calcination temperature from about 400 °C at 700 °C to around 200 °C at 1100 °C. The phenomenon of color-changing could be explained as follows: ZnO has typical crystal lattice defects such as oxygen vacancies. At high temperature, more and more oxygen vacancies emerge in ZnO due to the flowing away of oxygen atoms, which would lead to the absorption of the colour centre and then the samples become yellow gradually. However, the oxygen comes back upon cooling and the color recover at the same time. It was found that the color of pure crystalline ZnO can change from white to yellow when the temperature increases to >500 °C, and then transform from yellow to white upon cooling to room temperature. It means ZnO is reversible thermochromism material. Similar result has been reported in the literature [59]. A decrease in the color-changing temperature with increasing calcination temperatures is

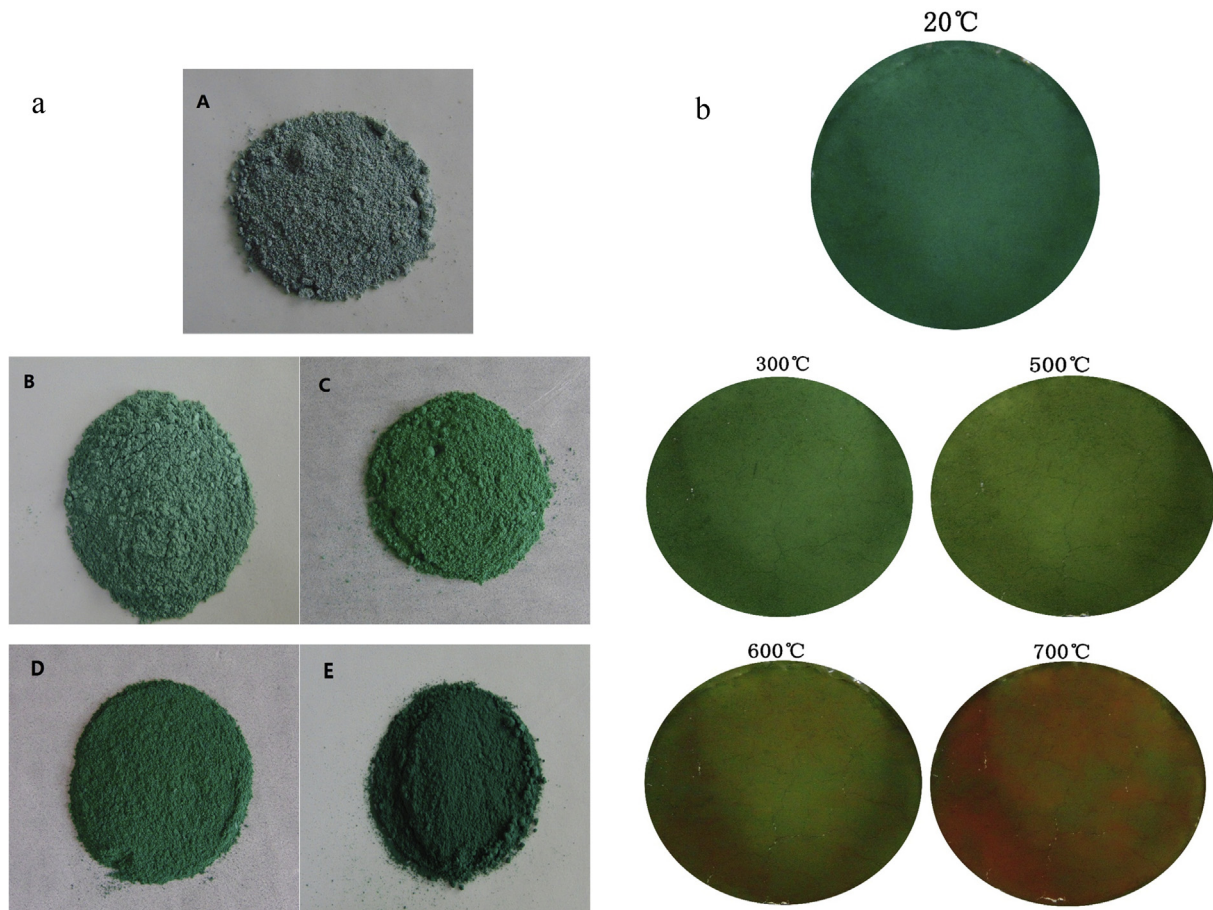


Fig. 8. (a) The color of Zn_{1-x}Co_xO samples with different sintering temperatures: A 700 °C; B 800 °C; C 900 °C; D 1000 °C; E 1100 °C; (b) the colour of the sample calcined at 900 °C under different test temperatures. (For interpretation of the references to colour in this figure legend, the reader is referred to the web version of this article.)

attributed to the decreased energy band gap, as evidenced by UV-vis absorption spectra and optical band gap analysis. From the XPS results, it can also be said that the high concentration of oxygen vacancies can induce the band gap narrowing and lead to the enhancement of visible light absorption capability. Similar result is also available [57]. The temperature dependency of the ZnO band gap energy (E_g) can be shown by the following equation, given by Ref. [60].

$$E_g(T) = E_g(0) - \frac{\alpha T^2}{T + \beta}$$

where, $E_g(T)$ is band gap energy of ZnO at TK, $\alpha = -5.5 \times 10^{-4} \text{ eV/K}$, $\beta = -900 \text{ K}$ and T is the temperature (in Kelvin). Based on the equation, it is seen that E_g decreases with the increase of temperature. Only when the photon energy ($h\nu$) is larger than the band gap E_g , could the optical absorption be emerged [61]. It probably was another reason that yellow ZnO becomes darker at higher testing temperature. These results confirm that the decrease of optical energy band gap is very beneficial to thermochromism properties. Thus, the properties have potential values in application of visible light and stealth materials.

3.9. Electrical resistivity measurements

Because the samples were in powder form, measured resistance are affected by the powder density and contacts between grains. Thus, the resistance of Zn_{1-x}Co_xO nanoparticles with a fixed weight

of 0.2 g were measured with a Φ2 mm mould under 5 MPa pressure. The resistivity can be calculated from the following equation:

$$\rho = RA/h$$

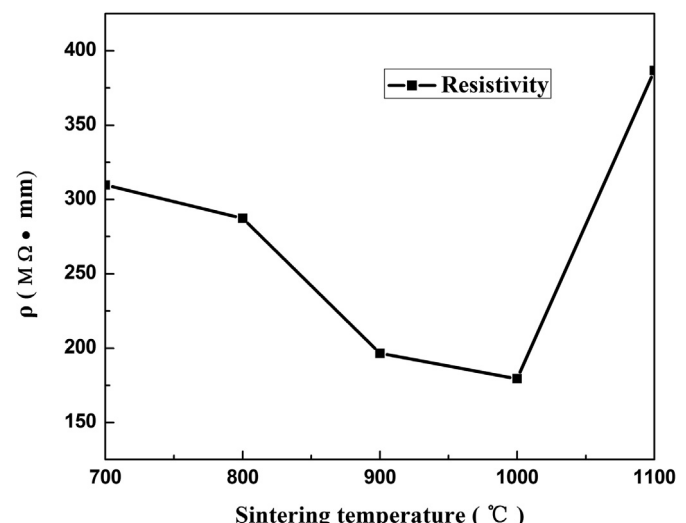


Fig. 9. The electric resistivity of Zn_{1-x}Co_xO samples with different sintering temperatures.

where ρ is the resistivity ($M\Omega \cdot mm$) of the powders, A is the cross sectional area (mm^2) and h is the thickness (mm) of the pressed $Zn_{1-x}Co_xO$ slice powders.

As shown in Fig. 9, the influences of sintering temperature on the electrical resistivity of $Zn_{1-x}Co_xO$ nanoparticles were investigated at room temperature. It can be observed that the resistivity of $Zn_{1-x}Co_xO$ nanoparticles shows a decreasing tendency initially with the increase of sintering temperature from 700 °C to 1000 °C. When the sintering temperature was increased to 1100 °C, the electrical resistivity of $Zn_{1-x}Co_xO$ nanoparticles increased, which means that the electrical conductivity decreased. The primary reason of the decrease in resistivity at low sintering temperature is attributed to the strengthened carrier mobility due to the improved crystalline quality. However, further increase of the sintering temperature leads to a finer grain and poor crystalline quality as evidenced by XRD and Raman spectra analysis. Obviously, the fine grain would result in more grain boundaries, along with more defects. Surface-roughness scattering and grain boundary scattering mainly lower the carrier mobility in $Zn_{1-x}Co_xO$ semiconductor nanoparticles and therefore the resistivity increased. Besides, the oxygen vacancies are deep donors and have high formation energies in n-type samples [62]. These oxygen vacancies cannot act as charge carriers to decrease resistivity, even though there is the highest concentration of oxygen vacancies of the sample calcinated at 1100 °C.

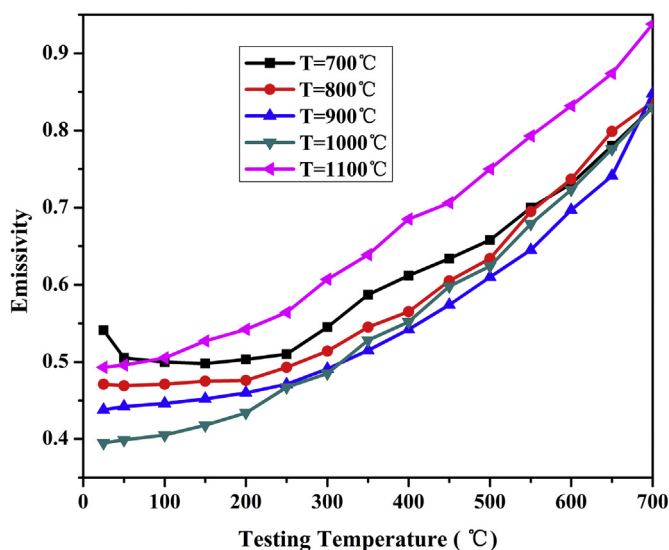


Fig. 10. Infrared emissivity of $Zn_{1-x}Co_xO$ samples under different test temperatures.

3.10. Infrared emissivity analysis

Fig. 10 shows the emissivity values at the wavelength of 3–5 μm of all the samples at various test temperatures from room temperature 20 °C to high temperature 700 °C, with an interval of 50 °C. It can be seen that the infrared emissivity decrease with the increase of sintering temperature from 700 °C to 1000 °C when the test temperature is 20 °C. This phenomenon may be caused by different morphology. Particles are loosely aggregated and nearly spherical at low sintering temperature while nuclei aggregate interact and nearly block at high calcination temperature. Nanoparticles with large specific surface area such as sphericity could enhance the infrared radiation absorption [63]. The model is shown in Fig. 11. Form Fig. 11a, it can be seen the sample is loosely spherical particles and most of the infrared radiation have been absorbed and only little radiation can be reflected. According to Kirchhoff's law, when a system is in the thermal equilibrium status, the absorbance is strictly equal to the emissivity. Thus, loosely spherical particles could lead to higher emissivity. When the particles aggregate interact and merge each other, as can be seen in Fig. 11b, the infrared radiation absorption decreases and infrared reflection increases and consequently lead to a lower emissivity. However, the infrared emissivity increases when calcination temperature reaches 1100 °C. The reason accounting for this phenomenon is the poor conductivity arisen from small particle size as well as poor crystallinity conductivity. The effect of conductivity on the infrared emissivity has been proved in previous works [64,65]. As was evidenced by electrical resistivity analysis, the poor crystalline quality leads to a higher emissivity [66].

The infrared emissivity values of the samples in 3–5 μm were measured at different test temperature, and the corresponding testing results are shown in Fig. 10. As seen from Fig. 10, the infrared emission values of the samples which were calcinated at 700 °C and 800 °C, rise at first and then reduce with the increased test temperature. This phenomenon could be explained as follows: the n-type donor carrier concentration of $Zn_{1-x}Co_xO$ semiconductor nanoparticles would increase with the increase of test temperature, which would cause the resistivity decrease [67]. Thus the infrared emissivity decrease at first with the improvement of conductivity [68]. Nevertheless, rotation and vibration of atoms and molecules would increase with the elevated test temperature. These changes could enhance the lattice vibrational absorption, and consequently lead to a higher absorption of infrared radiation. When the influence of lattice vibrational absorption on infrared emissivity is greater than that of conductivity, the emissivity would increase.

The infrared emissivity increases with the increase of test temperature from 20 °C to 700 °C when the powders are annealed at 900 °C, 1000 °C and 1100 °C. It may be due to the fact that the

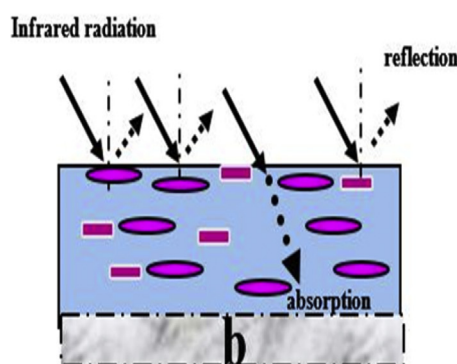


Fig. 11. Schematic diagram of infrared radiation behavior of samples with different morphology: a sphericity; b block.

impacts of lattice vibrational absorption were greater than that of conductivity in the test temperature range if the annealing temperature exceeds 900 °C. Besides, when the test temperatures vary from room temperature 20 °C to high temperature 700 °C, the changes of infrared emissivity at calcination temperatures of 700 °C, 800 °C, 900 °C, 1000 °C and 1100 °C is about 0.289, 0.362, 0.396, 0.412 and 0.422, respectively, which indicates that the changing rates of infrared emissivity has increased with the increase of calcination temperature. These results suggested that the sintering temperature is really a crucial factor for the infrared radiation properties of materials.

4. Conclusions

In summary, the green $Zn_{1-x}Co_xO$ nanopowders were prepared by solid-state reaction. XRD results confirm that the as-synthesized samples have hexagonal wurtzite structure, but the peaks of the secondary phase, Co_3O_4 , were observed when sintering temperature is 700 °C and 800 °C. Besides, the sintering temperature have an important impact on crystallite sizes, lattice parameters, volume of the unit cell and microstructure. EDS results provided strong evidence that Co ions substituted the Zn ions in the ZnO lattice. XPS analysis indicates that Co-ions are +2 state in ZnO lattice. It was found that with the increase of the sintering temperature, the area ratio of oxygen vacancies is increased. The optical energy band gap was found to decrease with the increase of sintering temperature, indicating a red shift. The results of colour and thermochromic analysis show that the color-changing temperature of $Zn_{1-x}Co_xO$ nanopowders is concerned with the energy band gap. The electrical resistivity of $Zn_{1-x}Co_xO$ nanoparticles relies on the crystallite sizes and crystallinity. The emissivity of $Zn_{1-x}Co_xO$ nanopowders not only relies on the morphology but also the electrical conductivity. In addition, the changing rates of infrared emissivity has increased with the increase of annealing temperature. As a novel kind of thermochromic materials, the $Zn_{1-x}Co_xO$ nanopowders have great potential applications in visible light stealth coatings and spacecraft thermal control coatings.

Acknowledgements

This work is financially supported by the National Natural Science Foundation of China (Grant No: 51403102), Fundamental Research Funds for the Center Universities (Grant No: NS2014058), Natural Science Foundation of Jiangsu Province, China (Grant No: BK20140811) and a Project Funded by the Priority Academic Program Development of Jiangsu Higher Education Institutions (PAPD).

References

- [1] L.-O. Hennerdal, M. Berggren, Picture-to-picture switching in full-color thermochromic paper displays, *Appl. Phys. Lett.* 99 (2011) 183303–183303-3.
- [2] O. Yarimaga, J. Jaworski, B. Yoon, J.-M. Kim, Polydiacetylenes: supramolecular smart materials with a structural hierarchy for sensing, imaging and display applications, *Chem. Commun.* 43 (2012) 2469–2485.
- [3] S.J. Zheng, Y. Xu, Q.H. Shen, H. Yang, Preparation of thermochromic coatings and their energy saving analysis, *Sol. Energy* 112 (2015) 263–271.
- [4] C.H. Wu, W.T. Qiu, J.B. Wang, M. Xu, L.X. Wang, Thermochromic property of $La_{0.8}Sr_{0.2}MnO_3$ thin-film material sputtered on quartz glass, *J. Alloy. Compd.* 506 (2010) L22–L24.
- [5] D.Q. Liu, W.W. Zheng, H.F. Cheng, H.T. Liu, Thermochromic VO_2 thin film prepared by post annealing treatment of V_2O_5 thin film, *Adv. Mater. Res.* 79–82 (2009) 747–750.
- [6] D.J. Watts, L. Battista, J. Junino, N. Colon, J. Federici, G. Thomas, Smart Coating System, 2006. US, US 20060182160 A1.
- [7] R.F. Reynolds, M.J. Kinsella, Thermal and Visual Camouflage System, 2002. US, US6338292 [P].
- [8] C.G. Granqvist, Electrochromics and thermochromics: towards a new paradigm for energy efficient buildings, *Mater. Today* 3 (2016) S2–S11.
- [9] D.S. Fan, Q. Li, Y.M. Xuan, Tailoring the solar absorptivity of thermochromic material $La_{0.7}Ca_{0.2}Sr_{0.1}MnO_3$, *Quant. Spectrosc. Ra* 112 (2011) 2794–2800.
- [10] Joel A. Johnson, John J. Heidenreich, Robert A. Mantz, Paul M. Baker, Michael S. Donley, A multiple-scattering model analysis of zinc oxide pigment for spacecraft thermal control coatings, *Prog. Org. Coat.* 47 (3–4) (2003) 432–442.
- [11] Parmanand Sharma, Amita Gupta, K.V. Rao, Frank J. Owens, Renu Sharma, Rajeev Ahuja, J. M. Osorio Guillen, Börje Johansson, G.A. Gehring, Ferromagnetism above room temperature in bulk and transparent thin films of Mn-doped ZnO , *Nat. Mater.* 2 (10) (2003) 673–677.
- [12] Y.M. Hao, S.Y. Lou, S.M. Zhou, Y.Q. Wang, X.L. Chen, G.Y. Zhu, R.J. Yuan, N. Li, Novel magnetic behavior of Mn-doped ZnO hierarchical hollow spheres, *J. Nanopart. Res.* 14 (2012) 1–9.
- [13] A.B. Djurišić, A.M.C. Ng, X.Y. Chen, ZnO nanostructures for optoelectronics: material properties and device applications, *Prog. Quantum Electron* 34 (2010) 191–259.
- [14] J.J. Chen, F. Zeng, D.M. Li, J.B. Niu, F. Pan, Deposition of high-quality zinc oxide thin films on diamond substrates for high-frequency surface acoustic wave filter applications, *Thin Solid Films* 485 (1–2) (2005) 257–261.
- [15] Y. Köseoglu, Enhanced ferromagnetic properties of Co-doped ZnO DMS nanoparticles, *J. Supercond. Nov. Magn.* 26 (2012) 485–489.
- [16] LL. Chen, Z.Z. Ye, J.G. Lu, H.P. He, B.H. Zhao, L.P. Zhu, Paul K. Chu, L. Shao, Codoping effects and electrical transport in In–N doped zinc oxide, *Chem. Phys. Lett.* 432 (1–3) (2006) 352–355.
- [17] H. Ohno, SEMICONDUCTORS: enhanced: toward functional spintronics, *Science* 291 (5505) (2001) 840–841.
- [18] T. Dietl, H. Ohno, F. Matsukura, J. Cibert, D. Ferrand, Zener model description of ferromagnetism in zinc-blende magnetic semiconductors, *Science* 287 (2000) 1019–1022.
- [19] S.D. Birajdar, V. Bhagwat, A. Shinde, K. Jadhav, Effect of Co^{2+} ions on structural, morphological and optical properties of ZnO nanoparticles synthesized by sol-gel auto combustion method, *Mater. Sci. Semicond. Process* 41 (2016) 441–449.
- [20] A.M. El Sayed, S. Taha, G. Said, Ahmed A. Al-Ghamdi, F. Yakuphanoglu, Structural and optical properties of spin coated $Zn_{1-x}Cr_xO$ nanostructures, *Superlatt. Microstruct.* 60 (2013) 108–119.
- [21] N. Srinatha, K.G.M. Nair, Basavaraj Angadi, Microstructure, electronic structure and optical properties of combustion synthesized Co doped ZnO nanoparticles, *Phys. B Condens. Matter* 474 (2015) 97–104.
- [22] M. Bouloudene, N. Viart, S. Colis, J. Kortus, A. Dinia, Antiferromagnetism in bulk $Zn_{1-x}Co_xO$ magnetic semiconductors prepared by the coprecipitation technique, *Appl. Phys. Lett.* 87 (2005) 052501.
- [23] R.D. Shannon, C.T. Prewitt, Effective ionic radii and crystal chemistry, *J. Inorg. Nucl. Chem.* 32 (5) (1970) 1427–1441.
- [24] Megha Vagadia, Ashish Ravalia, Uma Khachar, P.S. Solanki, R.R. Doshi, S. Rayaprol, D.G. Kuberkar, Size and grain morphology dependent magnetic behaviour of Co-doped ZnO , *Mater. Res. Bull.* 46 (11) (2011) 1933–1937.
- [25] A. Goktas, F. Aslan, I.H. Mutlu, Effect of preparation technique on the selected characteristics of $Zn_{1-x}Co_xO$ nanocrystallizing thin films deposited by sol–gel and magnetron sputtering, *J. Alloys. Compd.* 615 (2014) 765–778.
- [26] A. Franco, H.V.S. Pessoni, P.R.T. Ribeiro, F.L.A. Machado, Magnetic properties of Co-doped ZnO nanoparticles, *J. Magn. Magn. Mater.* 426 (2017) 347–350.
- [27] I.A. Sarvari, H. Salamati, P. Kameli, E.S. Razavi, Optical, structural, and magnetic properties of ZnO : Co nanoparticles prepared by a thermal treatment of ball milled precursors, *J. Supercond. Nov. Magn.* 24 (2011) 2295.
- [28] Fei Yi, Hai Zhu, Jason C. Reed, Ertugrul Cubukcu, Plasmonically enhanced thermomechanical detection of infrared radiation, *Nano Lett.* 13 (4) (2013) 1638–1643.
- [29] N. Adak, N. Heybeli, C. Ertekin, Infrared drying of strawberry, *Food Chem.* 219 (2016) 109–116.
- [30] W.G. Zhang, G.Y. Xu, R.Y. Ding, K.G. Duan, J.L. Qiao, Nacre biomimetic design—a possible approach to prepare low infrared emissivity composite coatings, *Mater. Sci. Eng. C* 33 (2013) 99–102.
- [31] H.J. Yu, G.Y. Xu, X.M. Shen, X.X. Yan, R. Huang, F.L. Li, Preparation of leafing Cu and its application in low infrared emissivity coatings, *J. Alloys Compd.* 484 (2009) 395–399.
- [32] J. Chen, Y.M. Zhou, Q.L. Nan, X.Y. Ye, Y.Q. Sun, F.Y. Zhang, Z.Q. Wang, Preparation and properties of optically active polyurethane/TiO₂ nanocomposites derived from optically pure 1,1'-binaphthyl, *Eur. Polym. J.* 43 (2007) 4151–4159.
- [33] Z.D. Nan, Q.Z. Jiao, Z.C. Tan, L.X. Sun, Investigation of thermodynamic properties of Co_2O_3 powder, *Thermochim. Acta* 404 (2003) 245–249.
- [34] F.T. Li, Q. Wang, J.Y.J. Hao, X.J. Wang, D. Zhao, S.Z. Qiao, Ionic liquid self-combustion synthesis of Bi₂O₃/Bi₂WO₆ heterojunctions with exceptional visible-light photocatalytic performances, *Nanoscale* 7 (2015) 1116.
- [35] J. Cao, B. Luo, H. Lin, B. Xu, S. Chen, Thermodecomposition synthesis of WO_3/H_2WO_4 heterostructures with enhanced visible light photocatalytic properties, *Appl. Catal. B-Environ.* 111 (2012) 288–296.
- [36] M. Shatnawi, A.M. Alsmadi, I. Bsoul, B. Salameh, G. Alnawashi, F. Al-Dweree, Magnetic and Optical properties of Co-doped ZnO nanocrystalline particles, *J. Alloy. Compd.* (2015) 655.
- [37] B. Pal, P.K. Giri, Defect mediated magnetic interaction and high T_c ferromagnetism in Co doped ZnO nanoparticles, *J. Nanosci. Nanotechnol.* 11 (2011) 9167–9174.
- [38] Richa Bhargava, Prashant K. Sharma, Ranu K. Dutta, Sanjeev Kumar, Avinash C. Pandey, Naresh Kumar, Influence of Co-doping on the thermal, structural, and optical properties of sol–gel derived ZnO nanoparticles, *Mater. Chem.*

- Phys.** 120 (2–3) (2010) 393–398.
- [39] A. Khorsand Zak, W.H. Abd Majid, M.E. Abrishami, Ramin Yousefi, X-ray analysis of ZnO nanoparticles by Williamson–Hall and size–strain plot methods, *Solid State Sci.* 13 (1) (2011) 251–256.
- [40] S.D. Birajdar, V. Bhagwat, A. Shinde, K. Jadhav, Effect of Co²⁺ ions on structural, morphological and optical properties of ZnO nanoparticles synthesized by sol-gel auto combustion method, *Mater. Sci. Semicond. Process.* 41 (2016) 441–449.
- [41] Jacek Wojnarowicz, Sylwia Kusnieruk, Tadeusz Chudoba, Stanislaw Gierlotka, Witold Lojkowski, Wojciech Knoff, Małgorzata I. Lukasiewicz, Bartłomiej S. Witkowski, Anna Wolska, Marcin T. Klepka, Tomasz Story, Marek Godlewski, Paramagnetism of cobalt-doped ZnO nanoparticles obtained by microwave solvothermal synthesis, *Beilstein J. Nanotechnol.* 6 (2015) 1957–1969.
- [42] B.D. Cullity, Elements of X-ray Diffraction, second ed., Addison-Wesley Publishing Company Inc, Reading, MA, 1978, pp. 277–279, 100–105.
- [43] K. Maaz, S. Karim, A. Mumtaz, S.K. Hasanaain, J. Liu, J.L. Duan, Synthesis and magnetic characterization of nickel ferrite nanoparticles prepared by co-precipitation route, *J. Magn. Magn. Mater.* 321 (12) (2009) 1838–1842.
- [44] G. Vijayaprasath, R. Murugan, T. Mahalingam, G. Ravi, Comparative study of structural and magnetic properties of transition metal (Co, Ni) doped ZnO nanoparticles, *J. Mater. Sci. Mater. Electron.* 26 (9) (2015) 7205–7213.
- [45] A. Goktasa, F. Aslan, A. Tumbul, S.H. Gunduz, Tuning of structural, optical and dielectric constants by various transition metal doping in ZnO: TM (TM=Mn, Co, Fe) nanostructured thin films: a comparative study, *Ceram. Int.* 43 (2017) 704–713.
- [46] S. Benramache, B. Benhaoua, H. Bentrah, Preparation of transparent, conductive ZnO: Co and ZnO: in thin films by ultrasonic spray method, *J. Nanost. Chem.* 3 (2013) 54.
- [47] C.J. Cong, J.H. Hong, K.L. Zhang, Effect of atmosphere on the magnetic properties of the Co-doped ZnO magnetic semiconductors, *Mater. Chem. Phys.* 113 (1) (2009) 435–440.
- [48] N.M. Alhada, E.B. Saion, A.H. Shaari, M.A. Kamarudin, M.H. Flaifel, S.H. Ahmad, S.A. Gene, A. Facile, Thermal-treatment route to synthesize ZnO nanosheets and effect of calcination temperature, *PLoS One* 9 (2014) 103–134.
- [49] G. van der Laan, C. Westra, C. Haas, G.A. Sawatzky, Satellite structure in photoelectron and Auger spectra of copper dihalides, *Phys. Rev. B* 23 (9) (1981) 4369–4380.
- [50] H.-J. Lee, C.H. Park, S.-Y. Jeong, K.-J. Yee, C.R. Cho, M.-H. Jung, D.J. Chadi, Hydrogen-induced ferromagnetism in ZnCoO, *Appl. Phys. Lett.* 88 (6) (2006) 062504.
- [51] Z.W. Dong, C.F. Zhang, H. Deng, G.J. You, S.X. Qian, Raman spectra of single micrometer-sized tubular ZnO, *Mater. Chem. Phys.* 99 (1) (2006) 160–163.
- [52] Z.K. Heiba, L. Arda, XRD, XPS, optical, and Raman investigations of structural changes of nano Co-doped ZnO, *J. Mol. Struct.* 1022 (2012) 167–171.
- [53] M. Fang, Z.W. Liu, Structure and properties variations in Zn_{1-x}Co_xO nanorods prepared by microwave-assisted hydrothermal method, *Mater. Sci. Semicond. Process.* 57 (2017) 233–238.
- [54] H.A. Weakliem, Optical spectra of Ni²⁺, Co²⁺, and Cu²⁺ in tetrahedral sites in crystals, *J. Chem. Phys.* 36 (1962) 2117–2140.
- [55] Faheem Ahmed, Nishat Arshi, M.S. Anwar, Rehan Danish, Bon Heun Koo, Effect of transition Metal (Co, Ni and Cu) doping on lattice volume, band gap, morphology and saturation magnetization of ZnO nanostructures, *J. Korean Phys. Soc.* 62 (10) (2013) 1479–1484.
- [56] S.K. Saha, M.A. Rahman, M.R. Sarkar, M. Shahjahan, M.K. Khan, Effect of Co doping on structural, optical, electrical and thermal properties of nanostructured ZnO thin films, *J. Semicond.* 36 (2015) 35–40.
- [57] J.P. Wang, Z.Y. Wang, B.B. Huang, Y.D. Ma, Y.Y. Liu, X.Y. Qin, X.Y. Zhang, Y. Dai, Oxygen vacancy induced band-gap narrowing and enhanced visible light photocatalytic activity of ZnO, *ACS Appl. Mater. Inter.* 4 (2012) 4024–4030.
- [58] Manuel García-Méndez, Álvaro Bedoya-Calle, Ricardo Rangel Segura, Víctor Coello, Investigation of the annealing effects on the structural and optoelectronic properties of RF-sputtered ZnO films studied by the Drude–Lorentz model, *Appl. Phys. A* 120 (4) (2015) 1375–1382.
- [59] G. Auer, W.D. Griebler, B. Jahn, Industrial Inorganic Pigments, third ed., Wiley-VCH Verlag GmbH & Co. KGaA, Weinheim, 2005.
- [60] Ü. Özgür, Yal. Alivov, C. Liu, A. Teke, M.A. Reshchikov, S. Doğan, V. Avrutin, S.-J. Cho, H. Morkoç, A comprehensive review of ZnO materials and devices, *J. Appl. Phys.* 98 (2005), 11–1.
- [61] J.P. Wang, Z.Y. Wang, B.B. Huang, Y.D. Ma, Y.Y. Liu, X. Qin, X.Y. Zhang, Y. Dai, Oxygen vacancy induced band-gap narrowing and enhanced visible light photocatalytic activity of ZnO, *ACS Appl. Mater. Inter.* 4 (2012) 4024–4030.
- [62] Anderson Janotti, Chris G. Van de Walle, Native point defects in ZnO, *Phys. Rev. B* 76 (2007) 165202.
- [63] Y.M. Zhu, Y.X. Han, X.Y. Wang, X. Wang, Preparation of nano- MgO and investigation of its infrared absorption properties, *Adv. Mater.* 58 (2008) 115–120.
- [64] Y.H. Yao, Q.X. Cao, Effect of preparation techniques on infrared emissivities of Zn_{0.9}Co_{0.1}O powders, *Mater. Sci. Semicond. Process.* 16 (2013) 759–764.
- [65] K.K. Wang, B. Cheng, B. Wu, C. Defranoux, P. Basa, C. Song, G. Han, Y. Liu, Study of annealing effects upon the optical and electrical properties of SnO₂:F/SiC_xO_y low emissivity coatings by spectroscopic ellipsometry, *Thin Solid Films* 571 (2014) 720–726.
- [66] H.J. Yu, G.Y. Xu, X.M. Shen, X.Y. Yan, W.G. Chen, Low infrared emissivity of polyurethane/Cu composite coatings, *Appl. Surf. Sci.* 255 (2009) 6077–6081.
- [67] S.D. Birajdar, P.P. Khirade, T.S. Saraf, R.C. Alange, K.M. Jadhav, Sol-gel auto combustion synthesis, electrical and dielectric properties of Zn_{1-x}Co_xO (0.0 ≤ x ≤ 0.36) semiconductor nanoparticles, *J. Alloys. Compd.* 691 (2017) 355–363.
- [68] F.L. Du, N. Wang, D.M. Zhang, Y.Z. Shen, Preparation, characterization and infrared emissivity study of Ce-doped ZnO films, *J. Raer Earth* 28 (2010) 391–395.